

# Chirality and Magnetic Configurations of Solar Filaments

Y. Ouyang<sup>1,2</sup>, Y. H. Zhou<sup>1,3</sup>, P. F. Chen<sup>1,3</sup>, and C. Fang<sup>1,3</sup>

<sup>1</sup> School of Astronomy & Space Science, Nanjing University, Nanjing 210023, China; [chenpf@nju.edu.cn](mailto:chenpf@nju.edu.cn)

<sup>2</sup> School of Science, Linyi University, Linyi 276000, China

<sup>3</sup> Key Lab of Modern Astron. & Astrophys. (Ministry of Education), Nanjing University, China

## ABSTRACT

It has been revealed that the magnetic topology in the solar atmosphere displays hemispheric preference, i.e., negative/positive helicity in the northern/southern hemisphere, respectively. However, the strength of the hemispheric rule and its cyclic variation are controversial. In this paper, we apply a new method based on filament drainage to 571 erupting filaments from 2010 May to 2015 December in order to determine the filament chirality and its hemispheric preference. It is found that 91.6% of our sample of erupting filaments follow the hemispheric rule of helicity sign. It is found that the strength of the hemispheric preference of the quiescent filaments decreases slightly from  $\sim 97\%$  in the rising phase to  $\sim 85\%$  in the declining phase of solar cycle 24, whereas the strength of the intermediate filaments keeps a high value around  $96 \pm 4\%$  all the time. Only the active-region filaments show significant variations. Their strength of the hemispheric rule rises from  $\sim 63\%$  to  $\sim 95\%$  in the rising phase, and keeps a high value  $82 \pm 5\%$  during the declining phase. Furthermore, during a half-year period around the solar maximum, their hemispheric preference totally vanishes. Besides, we also diagnose the magnetic configurations of the filaments based on our indirect method, and found that in our sample of erupting events, 89% are inverse-polarity filaments with a flux rope magnetic configuration, whereas 11% are normal-polarity filaments with a sheared arcade configuration.

*Subject headings:* Sun: activity — Sun: magnetic fields — Sun: filaments, prominences

## 1. Introduction

The magnetic field in the solar atmosphere, which is responsible for solar eruptions (Chen 2011), originates from the tachocline at the bottom of the convection zone, and rises up buoyantly out of the solar surface. Because of the antisymmetry of the Coriolis force, the magnetic structures in the solar atmosphere often display symmetry or antisymmetry between the northern and the southern hemispheres, i.e., the  $\alpha$ -effect. A typical example is the Joy's law (D'Silva & Choudhuri 1993; Wang & Sheeley 1991; Fan et al. 1994). On the other hand, the interaction between the buoyant flux tubes and the turbulent convection zone may weaken any hemispheric preference, i.e., the  $\Sigma$ -effect (Longcope et al. 1998a). In addition, there are other effects such as the surface motions and magnetic diffusion. As a result, the strength

of the hemispheric preference is expected to vary for different proxies of the magnetic topology. For example, in terms of the current helicity, it was found that about  $70 \pm 12\%$  of active regions follow the hemispheric rule (Seehafer 1990; Pevtsov et al. 1995; Abramenko et al. 1997; Bao & Zhang 1998; Hagino & Sakurai 2005; Zhang 2006; Hao & Zhang 2011; Gosain et al. 2013; Liu et al. 2014), i.e., the helicity is negative in the northern hemisphere and positive in the southern hemisphere. In terms of the sunspot whorls, although as high as 80% of the  $H\alpha$  whorls were found to be counterclockwise (measured inwardly) in the northern hemisphere and clockwise in the southern hemisphere (Hale 1927; Richardson 1941; Ding et al. 1987). However, it was noticed that only a small fraction of sunspots show a vortical structure (Richardson 1941), and most sunspot whorls include both clockwise and counterclock-

wise H $\alpha$  fibrils (Pvtsov et al. 2003). A similar complex situation happens to the X-ray sigmoids (Rust & Kumar 1996; Lim & Chae 2009), since they suffer from projection effects and even potential magnetic fields may also have similar shapes.

Another important proxy of the magnetic topology is the chirality of filament channels and their overlying coronal arcade, as proposed by Martin et al. (1992). Here the chirality of a filament channel is defined to be dextral/sinistral if the axial magnetic field of the filament is to the right/left when viewed from the positive polarity side of the filament channel. The chirality of filament channels originates from several sources, e.g., the twist of the magnetic field before emerging into the solar atmosphere, the interaction between two neighboring flux systems, and solar surface motions (van Ballegoijen & Martens 1989; Zirker et al. 1997; van Ballegoijen et al. 1998; Mackay et al. 2000). These sources are further divided into 8 mechanisms, each of which produces the chirality pattern consistent and/or inconsistent with the hemispheric rule (Yeates & Mackay 2009). Therefore, it is important to determine the percentage of solar filaments which follow the hemispheric rule. With a sample of 73 quiescent filaments, they found that  $\sim 80\%$  of them were either dextral (with negative helicity) in the northern hemisphere or sinistral (with positive helicity) in the southern hemisphere. In their paper, they also proposed a rule, called Martin’s rule hereafter, i.e., a dextral filament has right-bearing barbs, whereas a sinistral filament has left-bearing barbs. With such a one-to-one correspondence, one can immediately determine the chirality of a filament by looking at the H $\alpha$  image without the help of vector magnetograms. Applying this rule to the H $\alpha$  images during 2000–2001, Pevtsov et al. (2003) confirmed that  $\sim 83\pm 3\%$  of the quiescent filament follow the hemispheric rule of helicity. Compared to quiescent filaments, active-region filaments seem to have a weaker hemispheric preference in helicity. For instance, Pevtsov et al. (2003) found that only  $\sim 76\pm 1\%$  of active-region filaments follow the hemispheric rule. As an extreme result, Martin et al. (1994) stated that active-region filaments do not obey the hemispheric rule, with nearly half filaments being dextral or sinistral in each hemisphere. One might argue that the contradictory results between Martin et al. (1994)

and Pevtsov et al. (2003) are due to the small sample, e.g., only 31 filaments in the former. However, later investigations with bigger samples also led to opposing conclusions. For example, with 123 filaments, Yeates et al. (2007) found that 82% of all filaments follow the hemispheric rule, whereas Bernasconi et al. (2005) identified the chirality of 658 filaments with an automated detection method, and found that only 68% of them obey the hemispheric rule. Such a result of weak preference might be due to the limited resolution of the H $\alpha$  full-disk observations so that the automated method cannot work well. What is even worse, Martens et al. (2014) claimed that the hemispheric preference seems to disappear or reverse during parts of the declining phase.

The discrepancy between different researchers might be partly attributed to their chirality identification method, where the filament chirality is determined by the bearing sense of the filament barbs according to Martin’s rule. The resulting statistics is contaminated by three factors: (1) Projection effects: A left-bearing barb might be falsely identified to be right-bearing due to the projection effects. This problem becomes more serious as the filament is closer to the solar limb; (2) Limitation of Martin’s rule: As pointed out by Guo et al. (2010) and Chen et al. (2014), Martin’s rule is applicable to the filaments supported by a magnetic flux rope only. For filaments which are supported by a magnetic sheared arcade, the correspondence between the filament chirality and the bearing sense of the filament barbs would be opposite to the Martin’s rule; (3) Multi-sampling: The typical lifetime of a filament is weeks or even months. Therefore, some filaments might be counted several times depending on their lifetime. In order to determine the strength of the hemispheric preference of the filament chirality, a better chirality identification method should be applied. For example, Sheeley et al. (2013) proposed to use the “coronal cells” in the extreme ultraviolet (EUV) images of the Sun along with photospheric magnetograms to determine the chirality of the filament channel. This method is applicable when the coronal cells are clear.

Recently, Chen et al. (2014) proposed an indirect method to determine the chirality of a filament without the help of vector magnetograms, which is independent of the magnetic type of

the filament, i.e., of normal-polarity or inverse-polarity. This method is based on the observational fact that when a filament erupts, parts of the cold plasmas drain down along the two legs of the supporting magnetic field lines and impact the solar surface, forming two conjugate draining sites (Zhou et al. 2006; Tripathi et al. 2013; Chen et al. 2014). With respect to the magnetic polarity inversion line (PIL) or the filament spine, the conjugate draining sites are either left-skewed or right-skewed, corresponding to dextral or sinistral chirality, respectively. One of the advantages of this method is that the draining sites are well separated and are close to the solar surface (i.e., not suspended in the corona as the filament barbs), which do not suffer from the projection effects. Moreover, only the erupting stage of a filament is considered, by which a filament is sampled only once.

In this paper, we attempt to apply this new method to examine the strength of the hemispheric preference of filament chirality. The paper is organized as follows: The data sample and the chirality identification method are described in §2, the results are presented in §3, which are discussed in §4 before a summary in §5.

## 2. Data Sampling and Analysis

The *Solar Dynamics Observatory* (*SDO*) mission provides high-resolution EUV images and magnetograms, which are observed by the Atmospheric Imaging Assembly (AIA, Lemen et al. 2012) and the Helioseismic and Magnetic Imager (HMI, Scherrer et al. 2012), respectively. Since its launch in early 2010, the satellite has been monitoring the Sun continuously, covering both the rising and the beginning of the declining phases of solar cycle 24. Solar activities, including filament eruptions, were routinely recorded by the Heliophysics Event Knowledgebase (HEK, Hurlburt et al. 2012). From 2010 May 13 to 2015 December 31, there are more than 1000 erupting filaments/prominences. Roughly half of these events are prominences above or behind the limb (McCauley et al. 2015). With all these events excluded, 576 filaments are found to erupt on the disk. Among these events, only 5 erupting filaments have no clear draining sites. Therefore, a total of 571 erupting filaments are selected as

our sample. The *SDO/AIA* observes the Sun in seven EUV and three UV channels with a pixel size of  $0''.6$  and a high time cadence of 12 s. In this study we use the 304 Å, 171 Å, and 193 Å bandpasses in order to trace the filament eruptions and the brightenings associated with the filament drainage. These filament eruptions are also monitored by the *Global Oscillation Network Group* (*GONG*) in  $H\alpha$  (Harvey et al. 2011), where filament barbs can be clearly recognized in many of them.

When a filament erupts, generally two draining sites are visible in EUV images, and the filament chirality can be identified by the method proposed by Chen et al. (2014), i.e., the chirality of a filament is dextral when the draining sites are left-skewed, or sinistral when the draining sites are right-skewed. The application of this method is illustrated in Figure 1 and explained as follows: The top panels are the sketch maps of the cases with left skew of the draining sites (panel a, corresponding to dextral chirality) and right skew of the draining sites (panel e, corresponding to sinistral chirality), respectively, where the dashed lines mark the magnetic PIL, the shaded areas represent the filament spine, and the two circles in each panel mark the EUV brightenings associated with the filament drainage. Panels (b–c) display the evolution of an erupting filament with dextral chirality, whereas panels (f–g) display the evolution of an erupting filament with sinistral chirality. To apply this method, we first check the *SDO/AIA* images to obtain the locations of the brightenings associated with the filament draining, as marked by the circles in panels (c) and (g) of Figure 1. In many cases, the skew of the draining sites can then be determined. In some cases where the filament is curved and the two draining sites are too close to the magnetic PIL, we mark the locations of the draining sites on the *SDO/HMI* magnetogram, as shown by Figure 1(d, h). Here the magnetogram is derotated to the time of the EUV images. With the correspondence of the draining sites and the magnetic polarities, we can easily determine the skew of the draining sites, and hence the chirality of the filament. It is noted that our chirality identification method works well even when only one draining site is visible (Bi et al. 2014).

The validity of this chirality identification method is confirmed with small samples by

Ouyang et al. (2015) and Hao et al. (2016) who found that the results are in accordance with the vector magnetograms, the skew of the twin dimmings and the skew of flaring loops after filament eruption. For a large sample like the one in this paper, we also checked the chirality determined by the skew of the associated flaring loops in all the disk events, which was proposed by Martin & McAllister (1995). It is found that the results obtained by the two methods are exactly the same. It is also noted that the bright draining sites of erupting filaments would not be confused with flaring patches since the brightening is preceded by the dark draining filament materials, as indicated by Figures 3 and 7 in Ouyang et al. (2015). For all the events in our sample, we trace the draining filament materials to determine the bright draining sites.

### 3. Results

With the method described in §2, the chirality of 571 erupting filaments is then determined. The top panel of Figure 2 plots the chirality distribution of these filaments, where the horizontal axis is the time and the vertical axis is the latitude. In this panel, the blue diamonds correspond to the filaments with dextral chirality (hence negative helicity), and the red diamonds represent the filaments with sinistral chirality (hence positive helicity). It is found that 307 out of 324, i.e., 94.8%, filaments in the northern hemisphere have negative helicity, and 216 out of 247, i.e., 87.4%, filaments in the southern hemisphere have positive helicity. Put together, 91.6% of our sample of erupting filaments follow the hemispheric rule of helicity sign.

In comparison, we apply Martin’s rule to the same sample, i.e., to examine the sign of helicity based on the bearing sense of the filament barbs, which are observed by *GONG* H $\alpha$  telescopes. Among the 571 filaments, 7 events are not visible in H $\alpha$ . Following Pevtsov et al. (2003) and Jing et al. (2004), for the remaining 564 filaments, the sign of helicity is assigned to be negative/positive when the filament barbs are predominantly right-bearing/left-bearing. The resulting distribution of the helicity sign is displayed in the bottom panel of Figure 2 with the same coordinates as the top panel. Similar to the top panel,

the blue diamonds correspond to the filaments with dextral chirality (hence negative helicity), and the red diamonds represent the filaments with sinistral chirality (hence positive helicity). Among all the 564 H $\alpha$  filaments, it is found that 211 out of 322, i.e., 65.5%, of the filaments in the northern hemisphere have negative helicity, and 152 out of 242, i.e., 62.8%, filaments in the southern hemisphere have positive helicity. It should be noted that 76 filaments in the northern hemisphere and 66 filaments in the southern hemisphere have no discernable barbs. If we exclude all the H $\alpha$  filaments without identifiable barbs, it is found that 85.8% of the filaments in the northern hemisphere have negative helicity, and 86.4% of the filaments in the southern hemisphere have positive helicity. As a whole, 86.0% of all the filaments with clear barbs follow the hemispheric rule of helicity sign, which is 5.6% less than the value obtained by our method using the filament draining sites.

Following Engvold (1998), we divide the filaments in our sample into three types, i.e., (1) Quiescent ones, which are located in quiet regions with relatively weaker magnetic field, (2) Intermediate ones with one end in an active region and the other in the quiet region, and (3) Active-region ones, which are located inside an active region. It is found that among the 571 filaments, there are 379 quiescent filaments, 100 intermediate filaments, and 92 active-region filaments. Their time-latitude diagrams of the helicity sign are displayed in three rows of Figure 3, respectively, where the blue diamonds correspond to negative helicity, whereas the red diamonds to positive helicity. It is shown that the strength of the hemispheric rule is 93% for the quiescent filaments, 95% for the intermediate filaments, and 83% for the active-region filaments, respectively. On the right side of each row, we sum up the corresponding type of filaments with time and plot their latitude distribution in histograms. It is revealed that each type of the filaments have a bimodal distribution in latitude. Whereas the quiescent filaments are distributed more broadly in latitude, the other two types are more concentrated in low latitudes. It is also seen that the quiescent and the intermediate filaments that are against the hemispheric rule are concentrated near the equator, whereas the active-region filaments that are against the hemispheric rule are concentrated near

the latitude of  $\sim 20^\circ$  in each hemisphere.

## 4. Discussions

### 4.1. Strength of the Hemispheric Rule

It has been argued that the solar dynamo processes generate well-organized symmetric or antisymmetric magnetic patterns over the two hemispheres of the Sun (e.g., [Zirker et al. 1997](#); [Pevtsov et al. 2014](#)). Important parameters characterizing the magnetic topology are the helicity and handedness or chirality, which can be quantified from vector magnetograms and imaging observations. As a result, a hemispheric rule was revealed, i.e., the helicity tends to be negative in the northern hemisphere and positive in the southern hemisphere. However, the strength of the hemispheric rule changes with different proxies and even with different samples. As summarized by [Wang \(2013\)](#), the strength lies in the range  $\sim 62\%$ – $82\%$  for sunspot whorls ([Hale 1925](#); [Richardson 1941](#); [Pvtsov et al. 2003](#)),  $\sim 60\%$ – $82\%$  for vector magnetograms of active regions ([Pevtsov et al. 1995](#); [Abramenko et al. 1997](#); [Bao & Zhang 1998](#); [Longcope et al. 1998b](#); [Pevtsov et al. 2001](#); [Hagino & Sakurai 2005](#); [Zhang 2006](#)),  $\sim 64\%$ – $87\%$  for X-ray sigmoids ([Rust & Kumar 1996](#); [Canfield & Pevtsov 1999](#); [Lim & Chae 2009](#)),  $\sim 55\%$ – $76\%$  for active-region filaments ([Martin et al. 1994](#); [Pevtsov et al. 2003](#)), and  $\sim 82\%$ – $84\%$  for quiescent and intermediate filaments ([Martin et al. 1994](#); [Pevtsov et al. 2003](#); [Lim & Chae 2009](#)).

It should be pointed out that, for all these proxies, the sign of helicity or chirality may be mis-identified for different reasons, e.g., projection effects, Faraday rotation, and so on ([Xu et al. 2009](#)). In terms of the filament chirality, the traditional identification method is based on Martin’s rule, i.e., right-bearing barbs correspond to dextral chirality, and left-bearing barbs correspond to sinistral chirality ([Martin et al. 1992](#)). However, as pointed out by [Chen et al. \(2014\)](#), the Martin’s rule is valid only for the inverse-polarity filaments, i.e., those magnetically supported by a flux rope. For normal-polarity filaments, i.e., those supported by a sheared arcade, however, the one-to-one correspondence is opposite, i.e., right-bearing barbs correspond to sinistral chirality, whereas left-bearing barbs correspond to dextral chirality. Therefore, when the Martin’s rule

is applied to a normal-polarity filament, its chirality would be mis-identified. In order to estimate the strength of the hemispheric rule of filament chirality, in this paper we applied a new method proposed by [Chen et al. \(2014\)](#), which is based on the skew of the filament draining sites. It is found that 523 out of 571, i.e., 91.6%, erupting filaments during 2010–2015 follow the hemispheric rule. We further divided these filaments into quiescent, intermediate, and active-region types, and found that the strength of the hemispheric rule is 93% for the quiescent filaments, 95% for the intermediate filaments, and 83% for the active-region filaments, respectively. Compared to the previous studies ([Martin et al. 1994](#); [Pevtsov et al. 2003](#); [Bernasconi et al. 2005](#); [Yeates et al. 2007](#); [Lim & Chae 2009](#)), our estimates of the strength for the quiescent and the intermediate filaments are slightly higher, but our estimate of the strength for the active-region filaments is remarkably higher.

In order to more quantitatively compare our result with those obtained using Martin’s rule, we also applied the Martin’s rule to all our filament events. The bearing sense of the filament barbs is judged by the  $H\alpha$  images observed by the *GONG* network. It is found that there are no  $H\alpha$  observations for 7 events. For the remaining 564 filaments, 363, i.e., 64.3%, filaments follow the hemispheric rule. It should be noted that among the 564 filaments, 142, i.e., 25.2%, of them have no clear barbs, hence their chirality cannot be determined by the Martin’s rule. If we exclude these filaments, then 86.0% of all the filaments with clear barbs follow the hemispheric rule. Such a value is about 5.6% smaller than our estimate using filament draining sites.

Compared to some of the previous studies, our statistics shows a significantly stronger hemispheric preference of filament chirality, i.e., dextral in the northern hemisphere and sinistral in the southern hemisphere. For the quiescent filaments, [Martin et al. \(1994\)](#) analyzed 73 filaments and found that the strength of the hemispheric rule is 82%. Later, [Pevtsov et al. \(2003\)](#) analyzed 1436 filaments, which leads to similar strength, i.e., 83%. However, our estimate is as high as 93%. For the intermediate filaments, [Lim & Chae \(2009\)](#) found that the strength of the hemispheric rule is 84%. However, our estimate is up to 95%. For

the active-region filaments, whereas [Pevtsov et al. \(2003\)](#) estimated the strength of the hemispheric rule to be 76%, [Martin et al. \(1994\)](#) claimed that there is no hemispheric preference. However, we found that 83% of the active-region filaments follow the hemispheric rule. The reason for the remarkable difference is probably that the previous authors used the bearing sense of filament barbs to determine the chirality of the filaments, which would lead to misidentification of chirality when the filament is of the normal-polarity type, i.e., the corresponding magnetic configuration is a sheared arcade. That is to say, we cannot judge the chirality of a filament by the bearing sense of its barbs ([Chen et al. 2014](#); [Ouyang et al. 2015](#)), nor can we judge the chirality by the magnetic polarities of the two endpoints of a filament ([Hao et al. 2016](#)). On the contrary, the chirality can be visually determined by other patterns, such as the skew of the filament draining sites ([Chen et al. 2014](#)), the skew of coronal loops or flaring loops ([Martin 1998](#)), and the skew of the twin dimmings upon filament eruptions ([Jiang et al. 2011](#)).

#### 4.2. Cyclic Behavior of the Hemispheric Rule

It was proposed that the hemispheric rule might be time-dependent (e.g., [Sakurai & Hagino 2003](#); [Choudhuri et al. 2004](#); [Hao & Zhang 2011](#); [Yang & Zhang 2012](#); [Gosain et al. 2013](#)). However, the results were divergent. In terms of the current helicity, the violation of the hemispheric rule was claimed to happen in any phase of a solar cycle. For example, [Sakurai & Hagino \(2003\)](#), [Choudhuri et al. \(2004\)](#), and [Hagino & Sakurai \(2005\)](#) claimed that the hemispheric rule might be opposite near solar minimum. However, [Bao et al. \(2000\)](#) found that the hemispheric rule is opposite during the rising phase of solar cycle 23. On the contrary, [Hao & Zhang \(2011, 2012, 2013\)](#) suggested that the violation of the hemispheric rule happens in the declining phase of solar cycle 23.

In terms of the filament chirality, [Mackay & van Ballegoijen \(2001\)](#) theoretically predicted that the hemispheric rule may disappear during the declining phase of a solar cycle. [Martens et al. \(2014\)](#) applied an automated method to a big sample of filaments from 2001 to 2012. As a preliminary result, they showed that the hemispheric rule waxes and wanes. It is strongly present in 2001–2002 around

solar maximum, but reverses in 2006–2007, which was approaching solar minimum. At other times, it is wholly absent. Again, they determined the filament chirality by the Martin’s rule, which is valid only for the filaments that are magnetically supported by a flux rope according to [Chen et al. \(2014\)](#).

In this paper, we used the filament draining sites to determine the filament chirality. A quick look at our results in [Figure 3](#) immediately gives an impression that the hemispheric rule of the filament chirality roughly holds well from 2010 to 2015. In order to check the cyclic evolution of the strength of the hemispheric rule, we calculate  $f$ , the percentage of the filaments which follow the hemispheric rule each year, and plot its evolution in [Figure 4](#), where the top panel compares the strength of the hemispheric rule of all the filaments (*connected red squares*) with the smoothed sunspot number ([Clette et al. 2016](#)), and the bottom panel compares the strength of the hemispheric rule among quiescent filaments (*red squares*), intermediate filaments (*green squares*), and active-region filaments (*blue squares*). It can be seen that as a whole, the filament chirality follows the hemispheric rule very well, and the strength is  $\sim 90\%$  in the rising phase of solar cycle 24, though slightly decreases to  $\sim 87\%$  during the solar maximum and the declining phase. After dividing these filaments into three types, it is then found that the strength of the quiescent filaments decreases slightly from  $\sim 97\%$  in the rising phase to  $\sim 85\%$  in the declining phase, whereas the strength of the intermediate filaments keeps a high value around  $96 \pm 4\%$  from 2010 to 2015. Only the active-region filaments show significant variations. Their strength of the hemispheric rule rises from  $\sim 63\%$  to  $\sim 95\%$  in the rising phase, and keeps a high value  $82 \pm 5\%$  during the declining phase. However, during a period from 2013 June to 2014 January, which is around the solar maximum, the hemispheric preference totally vanishes. As seen from [Figure 3](#), whereas no active-region filaments erupt in the northern hemisphere during this period (marked by the two vertical dashed lines in the bottom panel of [Figure 3](#)), there are equal active-region filaments with dextral and sinistral chirality in the southern hemisphere. During this period, the sunspot area in the southern hemisphere reaches its highest peak

in solar cycle 24, whereas the sunspot area in the northern hemisphere reaches a local minimum (Deng et al. 2016).

Similar to our result, Bao et al. (2001) also found that the fraction of active regions with reversed helicity sign is higher near the solar maximum of solar cycle 22. We are still not sure whether the absence of the hemispheric rule of the active-region filaments (and hence the corresponding active regions, Wang et al. 2013) near solar maximum happens every solar cycle. However, it is interesting to notice that active regions that do not follow the hemispheric rule are generally more productive in solar flares (Bao et al. 2001).

### 4.3. Inverse- and Normal-polarity Filaments

Magnetic measurements indicate that solar filaments can be divided into (1) inverse-polarity filaments, whose magnetic field component perpendicular to the magnetic PIL is opposite to what expected from the photospheric magnetograms, and (2) normal-polarity filaments, whose magnetic orientation is the same as expected from the photospheric magnetograms (Leroy et al. 1984; Bommier & Leroy 1998). Theoretically, the two types of filaments are described by the KR model (Kuperus & Raadu 1974) and the KS model (Kippenhahn & Schlüter 1957), respectively. The former corresponds to a flux rope, whereas the latter corresponds to a sheared arcade. The original 2-dimensional models were later extended to 3-dimensions (Antiochos et al. 1994; Aulanier & Demoulin 1998; van Ballegoijen 2004). With solar filaments being the progenitor of coronal mass ejections (CMEs, Chen 2011), it is natural to think that the pre-eruption magnetic structure is a flux rope in some CME events, and a sheared arcade in other events (Gosling 1999; Chen 2011; Cheng et al. 2014; Song et al. 2014; Cheng et al. 2015), which was confirmed by Ouyang et al. (2015) in observations. However, we are still lacking the information on the percentage of the two types of solar filaments.

In 1980s, efforts were made to measure the magnetic field of solar prominences (Leroy et al. 1984; Bommier & Leroy 1998). According to Leroy et al. (1984),  $\sim 25\%$  of their  $>900$  measurements in a sample of 120 prominences correspond to the normal-polarity configuration. How-

ever, as they discussed in their paper, such a ratio is biased by several selection effects. Besides, there are different numbers of measurements for different prominences. With their result, we still do not know how many prominences have the normal-polarity configuration. Unfortunately, there were no systematic measurements of magnetic field for filaments/prominences in order to distinguish between inverse-polarity and normal-polarity configurations. However, recently Chen et al. (2014) proposed an indirect method to distinguish the two types of magnetic configurations, i.e., a dextral/sinistral filament with right-/left-bearing barbs respectively has an inverse-polarity configuration, whereas a dextral/sinistral filament with left-/right-bearing barbs respectively has a normal-polarity configuration.

This method can be summarized as follows: the filaments which obey Martin’s rule have the inverse-polarity configuration, whereas the filaments which disobey Martin’s rule have the normal-polarity configuration. In order to check the percentage of each type of filaments, we apply this method to our sample of 571 erupting filaments. Considering that 142 filaments have no clear barbs, we scrutinize the high-resolution *SDO/AIA* images to examine the bearing sense of the filament threads rather than the filament barbs, since filament threads are more reliable than filament barbs in determining the bearing direction (Martin et al. 2008). With the filament threads not identifiable in 7 filaments, we finally get a sample of 564 filaments, including 372 quiescent filaments, 100 intermediate filaments, and 92 active-region filaments. It is found that Martin’s rule and our new chirality identification method agree with each other for 503 out of 564, i.e., 89%, filaments, i.e., these filaments are magnetically supported by a flux rope, therefore are inverse-polarity filaments; However, Martin’s rule and our new method do not agree with each other for 61 out of 564, i.e., 11%, filaments, i.e., they are magnetically supported by a sheared arcade, therefore are normal-polarity filaments. Among the 61 normal-polarity filaments, there are 15 quiescent filaments, 9 intermediate filaments, and 37 active-region filaments. In another word, among our sample, 37 out of 92, i.e., 40%, active-region filaments are of the normal-polarity type, 9 out of 100, i.e., 9%, intermediate filaments are of

the normal-polarity type, and 15 out of 372, i.e., 4%, quiescent filaments are of the normal-polarity type. These results are illustrated by the diagrams in Figure 5.

It is noted here that in H $\alpha$  images, many filaments may have co-existing left-bearing and right-bearing barbs. Some are real, as discussed by Guo et al. (2010), others might be due to projection effects. In this section, we used filament threads to check the bearing sense, instead. It is found that only 6 filaments have co-existing left-bearing and right-bearing barbs. We take the dominant sense for each filament. It is interesting to notice that the minority threads in each filament are generally located near one end of the spine, and remain intact upon eruption.

## 5. Summary

In this paper, we performed statistical analyses on the chirality and the magnetic configurations (inverse-polarity versus normal polarity) of the solar filaments which erupt on disk from 2010 May 13 to 2015 December 31, covering both the rising phase and the beginning of the declining phases of solar cycle 24. The chirality is determined by an indirect method proposed by Chen et al. (2014), i.e., left-/right-skewed drainage corresponds to the dextral/sinistral chirality, respectively. The determination of the magnetic configuration is also based on a method proposed by Chen et al. (2014), i.e., those filaments that follow the Martin's rule (Martin et al. 1994) are of the inverse-polarity type, and those that disobey Martin's rule are of the normal-polarity type. By studying a sample of 571 filaments, we obtained the following results:

(1) About 94.8% of the filaments in the northern hemisphere have negative helicity, and 87.4% of the filaments in the southern hemisphere have positive helicity, indicating a significant hemispheric preference of helicity. As a whole, 91.6% of our sample of erupting filaments follow the hemispheric rule of helicity sign. With the improved method in determining the filament chirality, the strength of the hemispheric rule is higher than previous studies. It should be noted that the statistical result is based on the erupting filaments. Those filaments which do not erupt during the disk passage are not included in our sample.

(2) Following the conventional way, we divided the filaments into three types, i.e., quiescent type, intermediate type, and active-region type. It is shown that the strength of the hemispheric rule is 93% for the quiescent filaments, 95% for the intermediate filaments, and 83% for the active-region filaments, respectively.

(3) Regarding the cyclic behavior of the hemispheric preference, it is found that the strength of the quiescent filaments decreases slightly from  $\sim 97\%$  in the rising phase to  $\sim 85\%$  in the declining phase, whereas the strength of the intermediate filaments keeps a high value around  $96 \pm 4\%$  all the time. Only the active-region filaments show significant variations. Their strength of the hemispheric rule rises from  $\sim 63\%$  to  $\sim 95\%$  in the rising phase, and keeps a high value  $82 \pm 5\%$  during the declining phase. However, during a half-year period around the solar maximum, the hemispheric preference totally vanishes.

(4) It is found that in our sample of erupting filaments, 89% are inverse-polarity filaments, which are magnetically supported by a flux rope, whereas 11% are normal-polarity filaments, which are magnetically supported by a sheared arcade.

The authors thank the referee for constructive suggestions and the *SDO*, *GONG*, and the Heliophysics Events Knowledgebase (HEK) system teams for providing the data. This research was supported by the Chinese foundations NSFC (11533005 and 11025314) and Jiangsu 333 Project.

## REFERENCES

- Abramenko, V. I., Wang, T. J., & Yurchishin, V. B. 1997, *Solar Physics*, **174**, 291
- Antiochos, S. K., Dahlburg, R. B., & Klimchuk, J. A. 1994, *ApJ*, **420**, L41
- Aulanier, G., & Demoulin, P. 1998, *A&A*, **329**, 1125
- Bao, S., & Zhang, H. 1998, *ApJ*, **496**, L43
- Bao, S. D., Ai, G. X., & Zhang, H. Q. 2000, in IAU Joint Discussion, Vol. 7, IAU Joint Discussion
- Bao, S. D., Ai, G. X., & Zhang, H. Q. 2001, in IAU Symposium, Vol. 203, Recent Insights into the Physics of the Sun and Heliosphere: Highlights from SOHO and Other Space Missions, ed. P. Brekke, B. Fleck, & J. B. Gurman, 247
- Bernasconi, P. N., Rust, D. M., & Hakim, D. 2005, *Sol. Phys.*, **228**, 97
- Bi, Y., Jiang, Y., Yang, J., et al. 2014, *ApJ*, **790**, 100



- Bommier, V., & Leroy, J. L. 1998, in *Astronomical Society of the Pacific Conference Series*, Vol. 150, IAU Colloq. 167: *New Perspectives on Solar Prominences*, ed. D. F. Webb, B. Schmieder, & D. M. Rust, 434
- Canfield, R. C., & Pevtsov, A. A. 1999, *EOS Transactions*, **80**, 13
- Chen, P. F. 2011, *Living Reviews in Solar Physics*, **8**
- Chen, P. F., Harra, L. K., & Fang, C. 2014, *ApJ*, **784**, 50
- Cheng, X., Ding, M. D., & Fang, C. 2015, *ApJ*, **804**, 82
- Cheng, X., Ding, M. D., Zhang, J., et al. 2014, *ApJ*, **789**, L35
- Choudhuri, A. R., Chatterjee, P., & Nandy, D. 2004, *ApJ*, **615**, L57
- Clette, F., Lefèvre, L., Cagnotti, M., Cortesi, S., & Bulling, A. 2016, *Sol. Phys.*, [arXiv:1507.07803 \[astro-ph.SR\]](https://arxiv.org/abs/1507.07803)
- Deng, L. H., Xiang, Y. Y., Qu, Z. N., & An, J. M. 2016, *AJ*, **151**, 70
- Ding, Y. J., Hong, Q. F., & Wang, H. Z. 1987, *Sol. Phys.*, **107**, 221
- D’Silva, S., & Choudhuri, A. R. 1993, *A&A*, **272**, 621
- Engvold, O. 1998, in *Astronomical Society of the Pacific Conference Series*, Vol. 150, IAU Colloq. 167: *New Perspectives on Solar Prominences*, ed. D. F. Webb, B. Schmieder, & D. M. Rust, 23
- Fan, Y., Fisher, G. H., & McClymont, A. N. 1994, *ApJ*, **436**, 907
- Gosain, S., Pevtsov, A. A., Rudenko, G. V., & Anfinogentov, S. A. 2013, *ApJ*, **772**, 52
- Gosling, J. T. 1999, *Washington DC American Geophysical Union Geophysical Monograph Series*, **111**, 205
- Guo, Y., Schmieder, B., Démoulin, P., et al. 2010, *ApJ*, **714**, 343
- Hagino, M., & Sakurai, T. 2005, *PASJ*, **57**, 481
- Hale, G. E. 1925, *Proceedings of the National Academy of Science*, **11**, 691
- . 1927, *Nature*, **119**, 708
- Hao, J., & Zhang, M. 2011, *ApJ*, **733**, L27
- Hao, J., & Zhang, M. 2012, in *Astronomical Society of the Pacific Conference Series*, Vol. 456, *Fifth Hinode Science Meeting*, ed. L. Golub, I. De Moortel, & T. Shimizu, 69
- Hao, J., & Zhang, M. 2013, in *IAU Symposium*, Vol. 294, *Solar and Astrophysical Dynamamos and Magnetic Activity*, ed. A. G. Kosovichev, E. de Gouveia Dal Pino, & Y. Yan, 149
- Hao, Q., Guo, Y., Fang, C., Chen, P.-F., & Cao, W.-D. 2016, *RAA*, **16**, 001
- Harvey, J. W., Bolding, J., Clark, R., et al. 2011, in *Bulletin of the American Astronomical Society*, Vol. 43, *AAS/Solar Physics Division Abstracts #42*, 17.45
- Hurlburt, N., Cheung, M., Schrijver, C., et al. 2012, *Sol. Phys.*, **275**, 67
- Jiang, Y. C., Yang, J. Y., Zhang, J., & Wang, J. X. 2011, *J. of Phys. Sci. & Application*, **1**, 148
- Jing, J., Yurchyshyn, V. B., Yang, G., Xu, Y., & Wang, H. 2004, *ApJ*, **614**, 1054
- Kippenhahn, R., & Schlüter, A. 1957, *ZAp*, **43**, 36
- Kuperus, M., & Raadu, M. A. 1974, *A&A*, **31**, 189
- Lemen, J. R., Title, A. M., Akin, D. J., et al. 2012, *Sol. Phys.*, **275**, 17
- Leroy, J. L., Bommier, V., & Sahal-Brechot, S. 1984, *A&A*, **131**, 33
- Lim, E.-K., & Chae, J. 2009, *ApJ*, **692**, 104
- Liu, Y., Hoeksema, J. T., Bobra, M., et al. 2014, *ApJ*, **785**, 13
- Longcope, D. W., Fisher, G. H., & Pevtsov, A. A. 1998a, *ApJ*, **507**, 417
- . 1998b, *ApJ*, **507**, 417
- Mackay, D. H., Gaizauskas, V., & van Ballegooijen, A. A. 2000, *ApJ*, **544**, 1122
- Mackay, D. H., & van Ballegooijen, A. A. 2001, *ApJ*, **560**, 445
- Martens, P. C., Yeates, A. R., & Pillai, K. G. 2014, in *IAU Symposium*, Vol. 300, *Nature of Prominences and their Role in Space V*, 135
- Martin, S. F. 1998, *Sol. Phys.*, **182**, 107
- Martin, S. F., Bilimoria, R., & Tracadas, P. W. 1994, in *NATO Advanced Science Institutes (ASI) Series C*, Vol. 433, *NATO Advanced Science Institutes (ASI) Series C*, ed. R. J. Rutten & C. J. Schrijver, 303
- Martin, S. F., Lin, Y., & Engvold, O. 2008, *Sol. Phys.*, **250**, 31
- Martin, S. F., Marquette, W. H., & Bilimoria, R. 1992, in *Astronomical Society of the Pacific Conference Series*, Vol. 27, *The Solar Cycle*, ed. K. L. Harvey, 53
- Martin, S. F., & McAllister, A. H. 1995, in *Bulletin of the American Astronomical Society*, Vol. 27, *AAS/Solar Physics Division Meeting #26*, 961
- McCauley, P. I., Su, Y. N., Schanche, N., et al. 2015, *Sol. Phys.*, **290**, 1703
- Ouyang, Y., Yang, K., & Chen, P. F. 2015, *ApJ*, **815**, 72
- Pevtsov, A. A., Balasubramaniam, K. S., & Rogers, J. W. 2003, *ApJ*, **595**, 500
- Pevtsov, A. A., Berger, M. A., Nindos, A., Norton, A. A., & van Driel-Gesztelyi, L. 2014, *Space Sci. Rev.*, **186**, 285
- Pevtsov, A. A., Canfield, R. C., & Latushko, S. M. 2001, *ApJ*, **549**, L261
- Pevtsov, A. A., Canfield, R. C., & Metcalf, T. R. 1995, *ApJ*, **440**, L109
- Pvtsov, A. A., Balasubramaniam, K. S., & Rogers, W. J. 2003, *Advances in Space Research*, **32**, 1905
- Richardson, R. S. 1941, *ApJ*, **93**, 24
- Rust, D. M., & Kumar, A. 1996, *ApJ*, **464**, L199
- Sakurai, T., & Hagino, M. 2003, *Journal of Korean Astronomical Society*, **36**, S7
- Scherrer, P. H., Schou, J., Bush, R. I., et al. 2012, *Sol. Phys.*, **275**, 207
- Seehafer, N. 1990, *Sol. Phys.*, **125**, 219

- Sheeley, Jr., N. R., Martin, S. F., Panasenco, O., & Warren, H. P. 2013, *ApJ*, **772**, 88
- Song, H. Q., Zhang, J., Chen, Y., & Cheng, X. 2014, *ApJ*, **792**, L40
- Tripathi, D., Reeves, K. K., Gibson, S. E., Srivastava, A., & Joshi, N. C. 2013, *ApJ*, **778**, 142
- van Ballegoijen, A. A. 2004, *ApJ*, **612**, 519
- van Ballegoijen, A. A., Cartledge, N. P., & Priest, E. R. 1998, *ApJ*, **501**, 866
- van Ballegoijen, A. A., & Martens, P. C. H. 1989, *ApJ*, **343**, 971
- Wang, Y.-M. 2013, *ApJ*, **775**, L46
- Wang, Y.-M., & Sheeley, Jr., N. R. 1991, *ApJ*, **375**, 761
- Wang, Y.-M., Sheeley, Jr., N. R., & Stenborg, G. 2013, *ApJ*, **770**, 72
- Xu, H., Gao, Y., & Zhang, H. 2009, *SCPMA*, **52**, 1749
- Yang, S., & Zhang, H. 2012, *ApJ*, **758**, 61
- Yeates, A. R., & Mackay, D. H. 2009, *Sol. Phys.*, **254**, 77
- Yeates, A. R., Mackay, D. H., & van Ballegoijen, A. A. 2007, *Sol. Phys.*, **245**, 87
- Zhang, M. 2006, *ApJ*, **646**, L85
- Zhou, G. P., Wang, J. X., Zhang, J., et al. 2006, *ApJ*, **651**, 1238
- Zirker, J. B., Martin, S. F., Harvey, K., & Gaizauskas, V. 1997, *Sol. Phys.*, **175**, 27

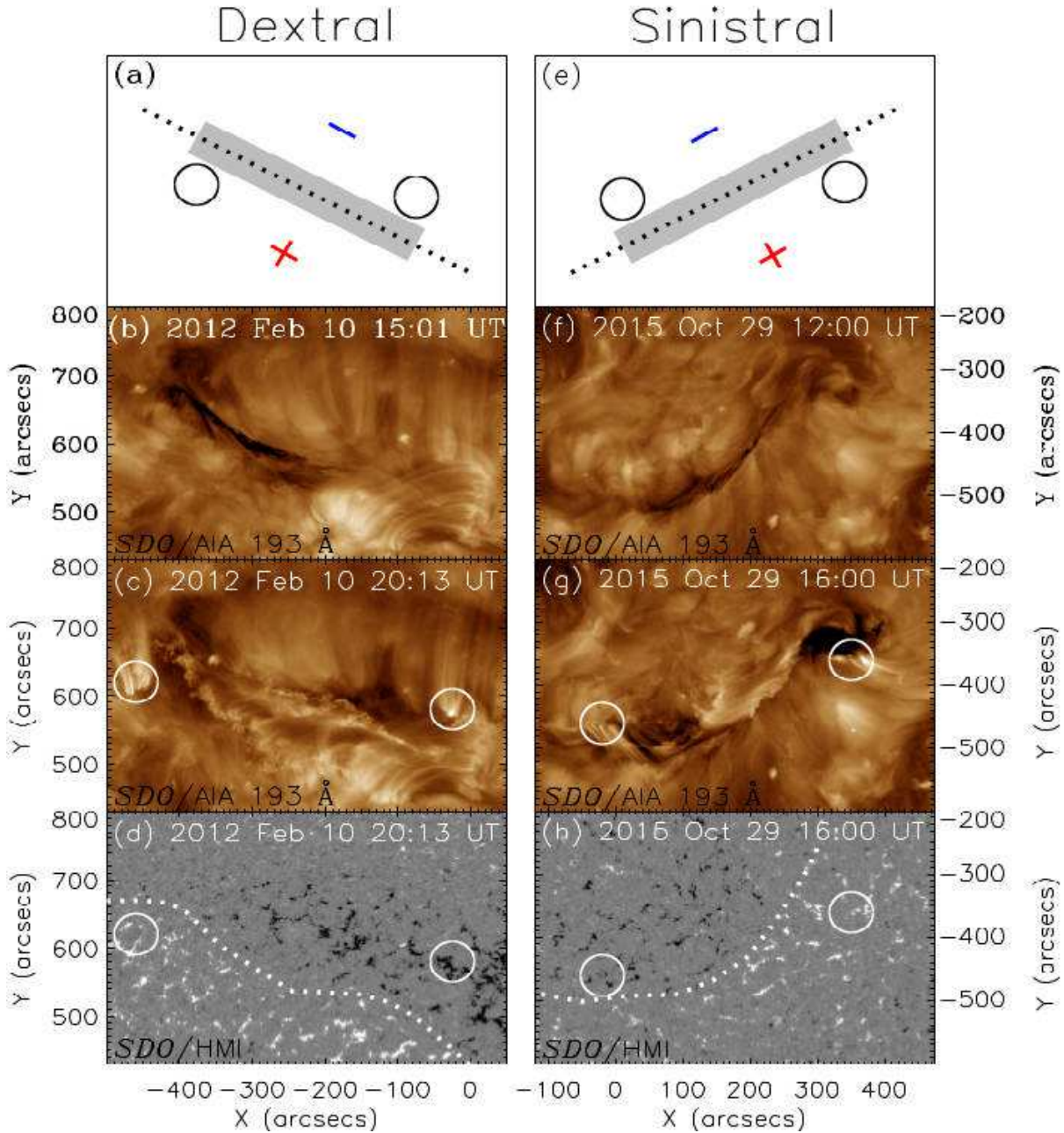
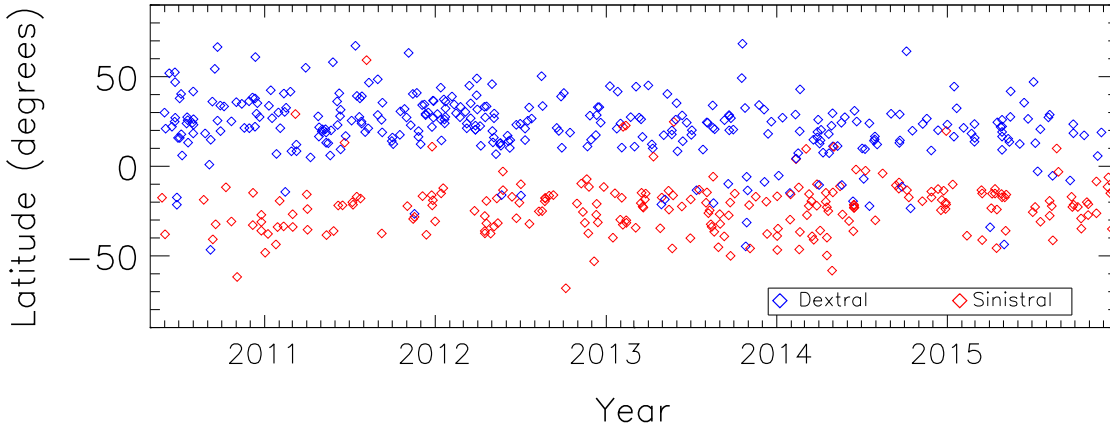


Fig. 1.— Description of our indirect method about how to determine the filament chirality by use of the filament draining sites. Top panels are the schematic sketches for a dextral (left) and a sinistral (right) filament, respectively. Panels (b–c) display the AIA 193 Å evolution of an erupting dextral filament, with two circles marking the conjugate draining sites, which are then located on the magnetogram in panel (d). It is seen that the two draining sites are left-skewed with respect to the magnetic PIL (white dashed line). Panels (e–h) are for the case of a sinistral filament, where the draining sites are right-skewed.

## Filament chirality determined by filament drainage



## Filament chirality determined by the Martin's rule

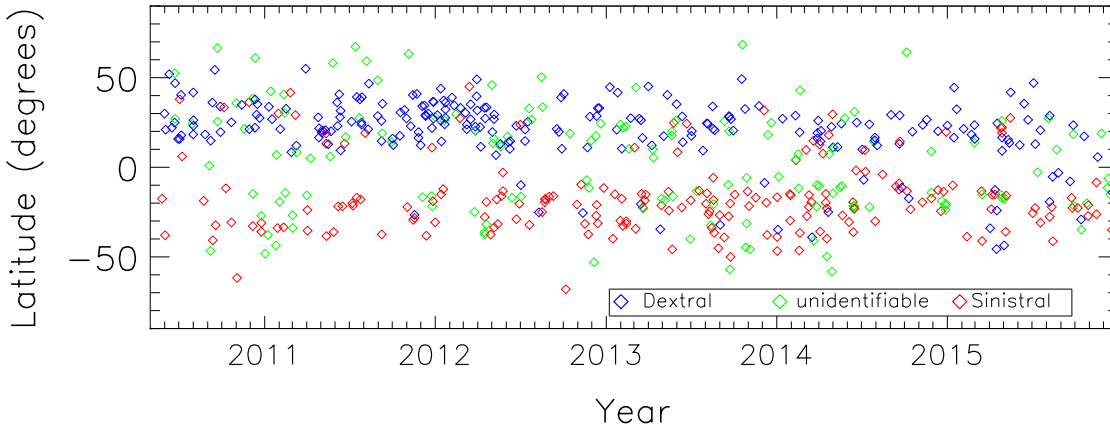
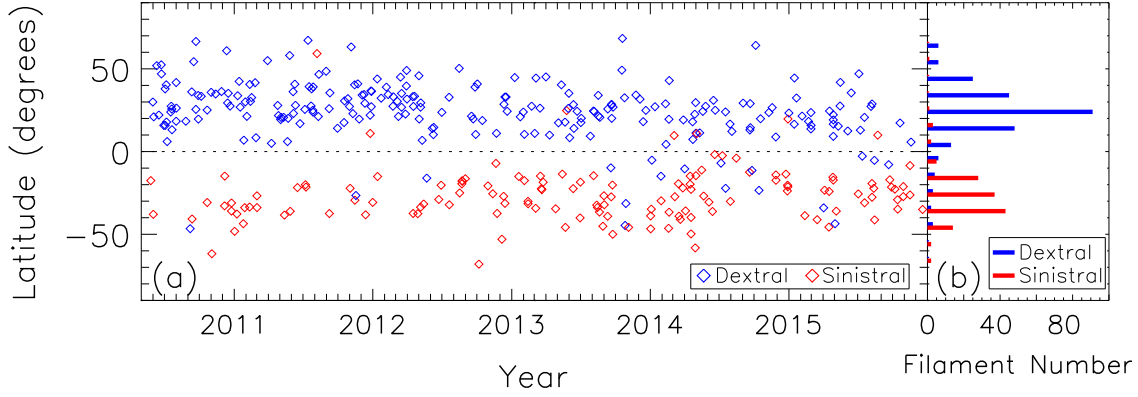
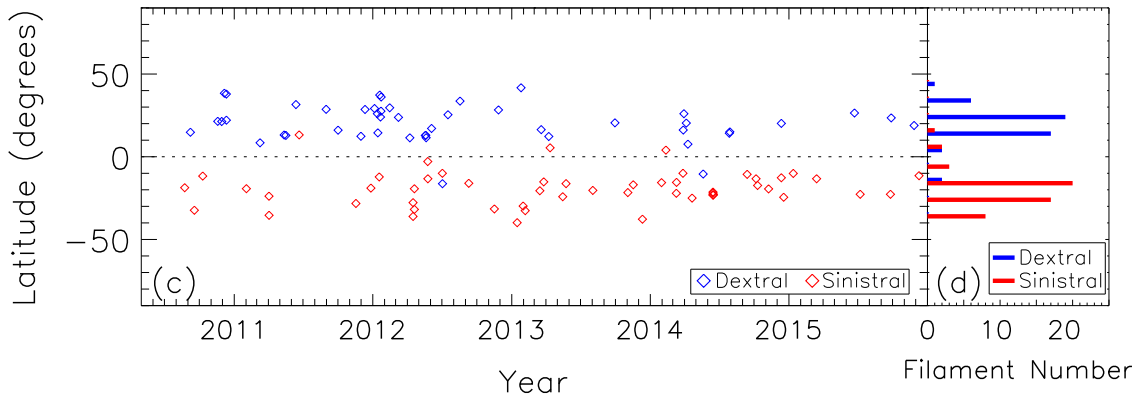


Fig. 2.— Top panel: The time-latitude distribution of chirality for the 571 erupting filaments observed from 2010 May to 2015 December, where the chirality is determined with the filament drainage method proposed by [Chen et al. \(2014\)](#), and the blue diamonds correspond to dextral chirality, whereas the red diamonds to sinistral chirality. Bottom panel: The same as the top panel except that the chirality is determined by the bearing sense of filament barbs as proposed by [Martin et al. \(1992\)](#), where the filaments without discernable  $H\alpha$  barbs (hence the filament chirality cannot be determined) are labeled with green diamonds.

### Quiescent Filaments



### Intermediate Filaments



### Active-region Filaments

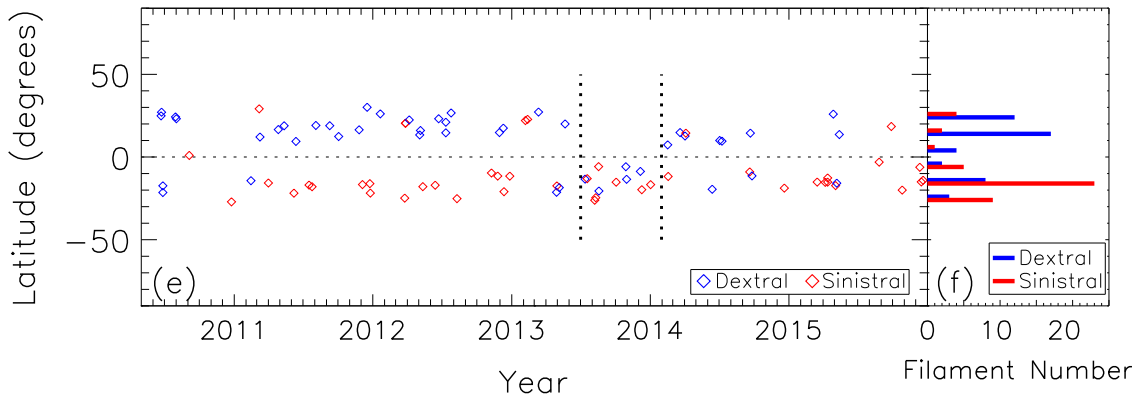


Fig. 3.— The time-latitude distribution of chirality for the 379 quiescent filaments (panel a), 100 intermediate filaments (panel c) and 92 active-region filaments (panel e), where the chirality is determined with the filament drainage method, and the blue diamonds correspond to dextral chirality, whereas the red diamonds to sinistral chirality. On the right side of each row, the filaments are summed over time to get the latitude distributions of the corresponding dextral and sinistral filaments.

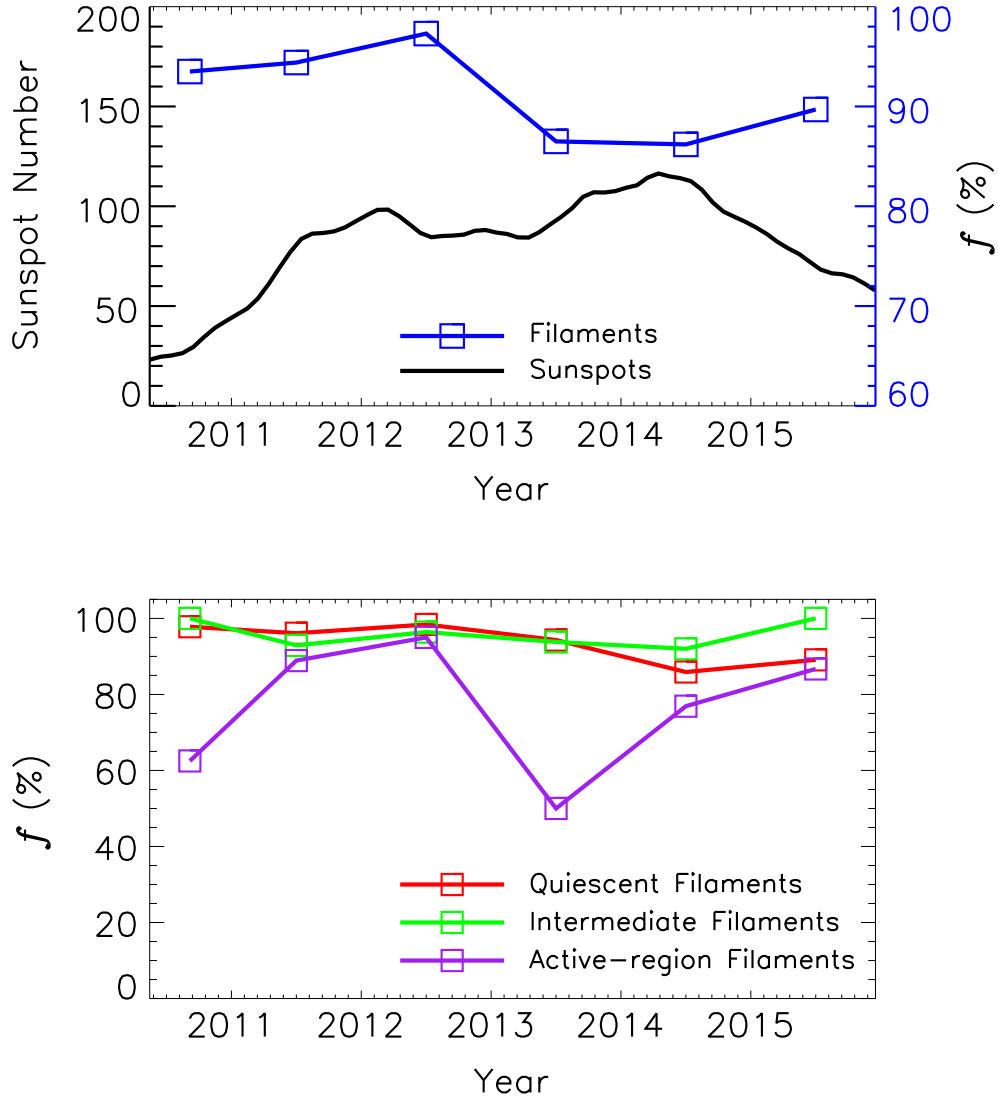


Fig. 4.— Top panel: Cyclic evolution of the sunspot number (black line) and  $f$ , the strength of the hemispheric rule obeyed by the filament chirality (connected blue squares). Bottom panel: Cyclic evolution of  $f$  for the quiescent filaments (connected red squares), intermediate filaments (connected green squares), and active-region filaments ((connected purple squares), where a level at 50% means that the hemispheric preference vanishes.

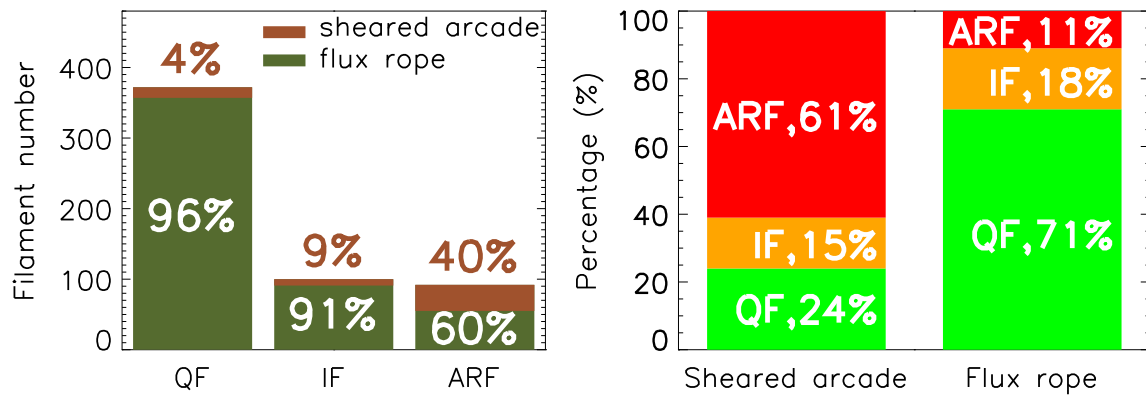


Fig. 5.— Left panel: The fractions of each type of filaments with a sheared arcade magnetic configuration (brown) and a flux rope configuration (green), where QF stands for quiescent filaments, IF for intermediate filaments, and ARF for active-region filaments. Right panel: The fractions of each type of magnetic configurations existing in quiescent filaments (green), intermediate filaments (orange), and active-region filaments (red).